creative commons
COMMONS DEED

저작자표시-비영리-변경금지 2.0 대한민국

이용자는 아래의 조건을 따르는 경우에 한하여 자유롭게

- 이 저작물을 복제, 배포, 전송, 전시, 공연 및 방송할 수 있습니다.

다음과 같은 조건을 따라야 합니다:



저작자표시. 귀하는 원저작자를 표시하여야 합니다.



비영리. 귀하는 이 저작물을 영리 목적으로 이용할 수 없습니다.



변경금지. 귀하는 이 저작물을 개작, 변형 또는 가공할 수 없습니다.

- 귀하는, 이 저작물의 재이용이나 배포의 경우, 이 저작물에 적용된 이용허락조건을 명확하게 나타내어야 합니다.
- 저작권자로부터 별도의 허가를 받으면 이러한 조건들은 적용되지 않습니다.

저작권법에 따른 이용자의 권리는 위의 내용에 의하여 영향을 받지 않습니다.

이것은 이용허락규약(Legal Code)을 이해하기 쉽게 요약한 것입니다.

Disclaimer

dCollection

공학석사학위논문

이륙 비행 하는 장수풍뎅이의 겉날개-속날개 상호작용

Interaction of the elytra and hind wings of a rhinoceros beetle (*trypoxylus dichotomus*) during take-off

2016 년 2 월

서울대학교 대학원

기계항공공학부

오 승 영

이륙 비행 하는 장수풍뎅이의 겉날개-속날개 상호작용

Interaction of the elytra and hind wings of a rhinoceros beetle (*trypoxylus dichotomus*) during take-off

지도교수 최 해 천

이 논문을 공학석사 학위논문으로 제출함

2016 년 1 월

서울대학교 대학원
기계항공공학부
오 승 영

오승영의 공학석사 학위논문을 인준함

2016 년 1 월

위 원 장 김 호 영

부위원장 최 해 천

위 원 박 형 민

Interaction of the elytra and hind wings of a rhinoceros beetle (*trypoxylus dichotomus*) during take-off

Seung Young Oh

Department of Mechanical & Aerospace Engineering

Seoul National University

Abstract

The elytra are a pair of hardened wings that cover the abdomen of a beetle to protect beetle's hind wings. During take-off, these elytra open and flap in phase with the hind wings. We investigated the effect of the elytra flapping on the beetle's aerodynamic performance. Numerical simulations are performed at Re=17,000 (based on the maximum velocity at wing tip and the mean chord length of the hind wing of a rhinoceros beetle during take-off) using an immersed boundary method. The simulations are focused on take-off, and the wing kinematics used are directly obtained from experimental observations using high speed cameras. The simulation results shows the three-dimensional vortical structures generated by the hind wing of the beetle and their interaction with the elytra. The presence of elytra has no effect on the lift generated by the hind wings, and the lift force on the elytra themselves is negligible.

Keywords: rhinoceros beetle, flapping wing, wing-wing interaction, insect flight, take-off mode, vortical structures, lift, circulation

Student number: 2014-21568

Contents

Abstract i

Contents iii

List of Figures iv

Nomenclature vi

Chapter

1 Introduction 1

2 Numerical Details 3

2.1 Numerical methods 3

2.2 Wing configurations and computational domain 3

2.3 Wing kinematics 5

3 Numerical Results and Discussion 9

3.1 Vortical structures and force coefficients 9

3.2 Iso-pressure surface 10

3.3 Vorticity fields at the cross-sections of the hind wing 11

4 Code Validation 16

4.1 Experimental setup 16

4.2 Validation result 17

5 Summary and Conclusion 24

Bibliography 25

List of Figures

FIGURE 2.1 Morphological features of an elytron (top left) and a hind wing (top right), and their relative position during take-off (bottom) · · · · · · · · · · · · · · · · · · 6

FIGURE 2.2 Computational domain and grid distribution · · · · · 7

FIGURE 2.3 Measured wing kinematics · · · · · · · · · · · · · 8

FIGURE 3.1 Instantaneous vortical structures (λ_2 vortex definition of Jeong & Hussain) at six different phases · · · 12

FIGURE 3.2 Iso-pressure surface of $p^*=-1.5$ over the hind wing at three different phases viewed from the upper surface of the hind wing: with the presence of elytra (upper), with the absence of elytra (lower) · · · · · · · · · 13

FIGURE 3.3 Time history of vertical force coefficients (upper) and horizontal force coefficients (lower) · · · · · · 14

FIGURE 3.4 Contour of the instantaneous span-wise vorticity at a span-wise location of R=0.25r, and their velocity vector during pronation for the case with the elytra (upper), and without the elytra (lower) · · · · · · 15

FIGURE 4.1 Computational domain and grid distribution for the code validation and grid dependency test (left) and experimental setup for the code validation (right) · 19

FIGURE 4.2 Modelled wing kinematics implemented for the code validation case and grid dependency test · · · · · 20

FIGURE 4.3 vertical force coefficient (upper) and horizontal force coefficient obtained for the grid dependency test (lower) · 21

FIGURE 4.4 Leading edge vortex identification at the cross-section of the hind wing at spanwise location of R=0.5r(upper), and a graph showing strength of leading edge vortex at three different phases (lower) · 22

FIGURE 4.5 Variation of circulation values with different number of instantaneous field is used for the phase averaging · 23

Nomenclature

Roman Symbols

C_D	drag coefficient
C_L	lift coefficient
C_V	vertical force coefficient
C_{V_H}	vertical force coefficient of hind wing without the presence of elytron
C_{V_HE}	vertical force coefficient of hind wing with the presence of elytron
C_H	horizontal force coefficient
C_{H_H}	horizontal force coefficient of hind wing without the presence of elytron
C_{H_HE}	horizontal force coefficient of hind wing with the presence of elytron
c	chord length
$\bar{c}$	mean chord length
f_i	momentum forcing
f	flapping frequency
F_V	vertical force
F_H	horizontal force
L	wing length
N_x, N_y, N_z	number of grid points
p	pressure
q	mass source/sink

Re	Reynolds number
S	wing surface area
t	time
T	flapping period
U	reference velocity (=maximum wing tip velocity)
u,v,w	streamwise, wall-normal and spanwise velocity components, respectively
x,y,z	Cartesian coordinate (streamwise, wall-normal, spanwise direction)

Greek Symbols

α	angle of attack
β	stroke plane angle
ν	kinematic viscosity of air
ρ	density of air
ϕ	flapping angle
ϕ_a	stroke amplitude
θ	pitching angle
ψ	deviation angle

Subscripts and superscripts

$(\,)_e$	elytra
$(\,)^*$	non-dimensionalized quantity
$\overline{(\,)}$	mean quantity

Chapter 1

Introduction

Since the late 1990s, micro aerial vehicles (MAVs) have attracted interest in the field of engineering and science. A typical MAV has a wing span of less than 15cm, a mass of less than 100g, and flyers at Reynolds number of less than Re=100,000 . At this flow regime, a fixed wing loses efficiency, however flapping wings become more efficient due to the unsteady flow mechanisms (Spedding & Lissaman, 1998; Ho *et al.*, 2003). Therefore a flapping wing is the preferred propulsion method for small flyers such as MAVs.

In 1996, Tennekes suggested a universal law relating the wing loading to the weight of a variety of flyers including flying insects, birds and airplanes. The definition of wing loading is defined as the weight of the flying object over the wing area. Assuming that flyers have geometrically similar shaped wings, the law relates the wing loading to weight of the flying object using the 1/3 power law. According to this law, species of dragonflies, such as, the green dragonfly and the yellow-banded dragonfly, have relatively low wing loading. On the other hand, species such as, the rhinoceros beetle and the fruit fly have relatively high wing loading. A larger wing loading allows the flyers to carry a larger payload, therefore it increasing the economy of the mission (Ho *et al.*, 2003). The rhinoceros beetle is one of the heaviest species and it has the highest wing loading among the flyers that satisfy the weight and size requirements of MAV.

There have been many attempts to explain the unsteady flow mechanisms related to flapping wings. One of most important factors affecting its aerodynamic performance is known to be the leading edge vortex (Birch & Dickinson, 2001; Ellington *et al.*, 1996). It is the helical vortical structure that forms at the upper surface of wing's leading edge during the translational motion that creates the low pressure region above the wing surface. Lu *et al.*, described in detail the generation and breakdown of the leading edge vortex for the case of dragon fly. Delayed stall mechanism prevents the immediate separation of leading edge vortex even at high AOA, therefore increasing the lift force during the translational motion (Ellington 1984). During the stroke reversal, there are other unsteady flow mechanisms considered to be important. Added mass is a force term related to the acceleration of the wing. Having high acceleration during the stroke reversal leads to a sudden increase in lift and drag forces (Sun & Tang 2002). In 1999 Dickinson suggested the wake capture mechanism, which demonstrates that the sudden increase in lift force during the stroke reversal is caused by the wake generated from the previous stroke. Many of the studies consider the flexible wing. Medina *et al.*, elucidated the effect of wing root and tip flexibility by introducing prescribed deformation at low Reynolds number ($\sim 10^3$) resulting in decrease in lift coefficient, however increase in efficiency.

In the present study, the interaction of the elytra and hind wings of a beetle during take-off has been considered. Horizontal and vertical forces generated by the hind wing are compared for the case with and the case without the presence of elytra. Code validation has been completed by comparing the circulation values with the experimental results at three different phases.

Chapter 2

Numerical Details

2.1 Numerical methods

Numerical simulations were performed on two pairs of flapping wings; the elytra and the hind wings. In the present study, the take-off mode from an upright standing rod was considered. An immersed boundary method (Kim, Kim & Choi, 2001) was used to analyze the flow characteristics around the elytra and the hind wings of a beetle. This method satisfies the no-slip condition at the moving body surface by including momentum forcing term and mass source/sing term to the Navier-Stokes and continuity equations. The resulting governing equations are given as

$$\frac{\partial u}{\partial t} + \nabla \cdot (uu) = -\nabla p + \frac{1}{\mathrm{Re}} \nabla^2 u + f_i, \tag{2.1}$$

$$\nabla \cdot u - q = 0, \tag{2.2}$$

where p is pressure, f_i is momentum forcing, q is mass source/sing and u is the flow velocity. A direct numerical simulation was performed, which requires no turbulence modeling. The simulations were performed at Reynolds number of 17,000 based on the mean chord length and the maximum hind wing velocity at the wing tip of an actual rhinoceros beetle during take-off.

2.2 Computational domain and boundary conditions

In order to obtain the morphological data of an elytron, a 3D

scanning technique was adopted. Then, a ray-casting method was applied to implement the 3D scanned elytron into the computational domain. The hind wing was modeled as a rigid flat plate. Figure 2.1 shows the morphological features of the elytra and the hind wing, and the wing configurations of a beetle and their relative wing positions during take-off. The lengths of the hind wing and the elytron are $3.3\bar{c}$ and $1.6\bar{c}$ respectively, where $\bar{c}$ is the mean chord length of hind wing, which is 15.6mm. The body of the beetle is tilted towards the ventricle side during take-off, so, the root of elytra is positioned directly above the root of the hind wing. Differences in their wing root positions in y-direction and x-direction are 6mm and 3mm respectively. Figure 2.2 shows the computational domain and the implemented elytron and hind wing. Wing motions are determined using three angles, which are the flapping angle, the pitching angle and the deviation angle. The flapping angle is the rotation of a wing about the z-axis. The pitching angle is the rotation of a wing about its pitching axis. In this study, the pitching axis is defined as a line connecting the root of the wing to the wingtip. The deviation angle is the angle between the pitching axis and the stroke plane angle. In this study, the stroke plane angle is assumed to be zero as its angle is close to zero and its variation is also minor. Therefore the stroke plane is same as the xy plane. The definition of each angle is illustrated in figure 2.2. For the boundary conditions, symmetric boundary condition was applied on the left wall. Therefore it assumes that two pairs of wings are flapping symmetrically about the left wall. On the other walls, far-field boundary conditions were applied. The size of the computational domain is $-1 < x/\bar{c} < 30,\ -30 < y/\bar{c} < 20,\ -25 < z/\bar{c} < 25$. The number of

grid points are $545 \times 289 \times 293$ in x−,y−, and z−directions respectively. The total number of grid points are 46 million. The grid dependency test had been performed beforehand at Reynolds number of 17,000, as explained in section 4.2.

2.3 Wing kinematics

To perform the numerical simulations, directly measured wing kinematics were implemented to describe the motions of the wings. Wing kinematics during take−off were measured by Lee *et al.*, (2015). Figure 2.3 shows the original wing kinematics data. In order to utilize the original data, quintic smooth spline was applied to connect the dots. Quintic spline uses 5th order polynomial for the angular position in order to make the angular acceleration the 3rd order polynomial, therefore the angular acceleration varies smoothly at every point. It is important to have the smooth acceleration terms as the 'added mass' term, which is determined by the acceleration, is one of the significant factors that affects the lift and drag forces of flapping wings ().To minimize the random error that arises from the measurements, Gaussian filter is adopted.

The average stroke amplitude of the hind wing over four periods is 172.6° and its flapping frequency (f) is 41.7Hz. The mass of the beetle used for the measurement of the wing kinematics is 5.9g. The hind wing's deviation angle is nearly constant for the 3^{rd} and 4^{th} strokes, and the pitching motion of elytra is negligible, therefore those two angles are assumed to be constant as 0° and 90°, respectively.

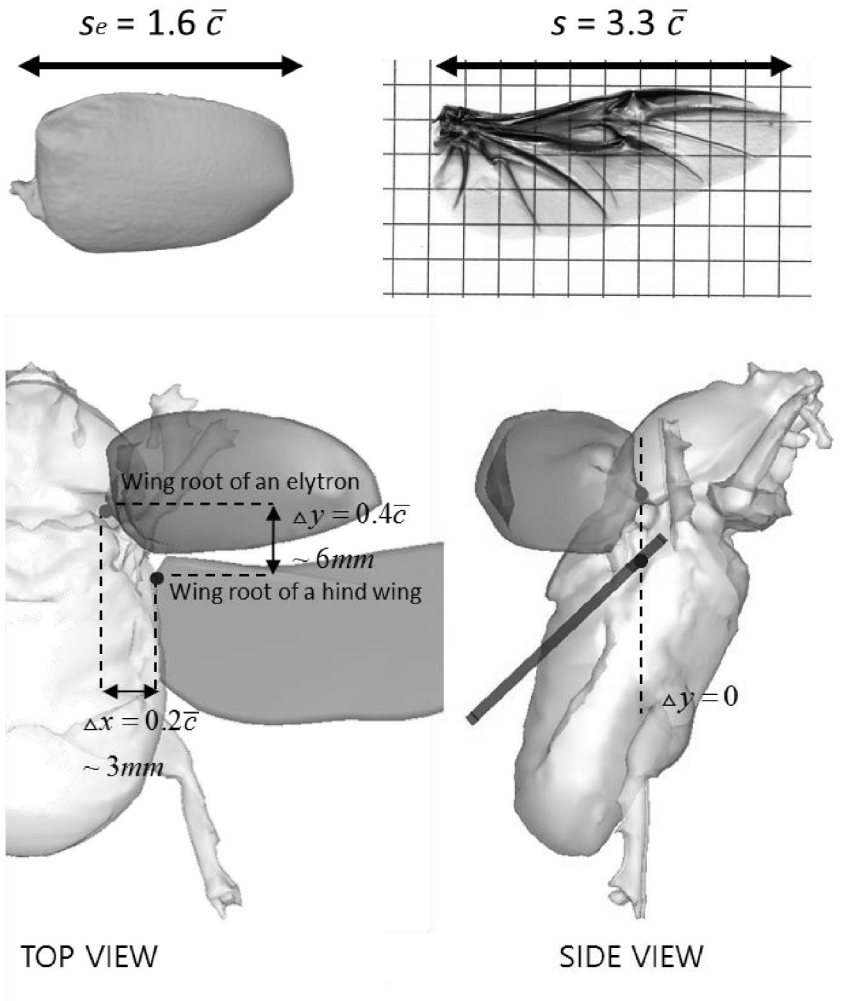


FIGURE 2.1 Morphological features of an elytron (top left) and a hind wing (top right), and their relative position during take-off (bottom).

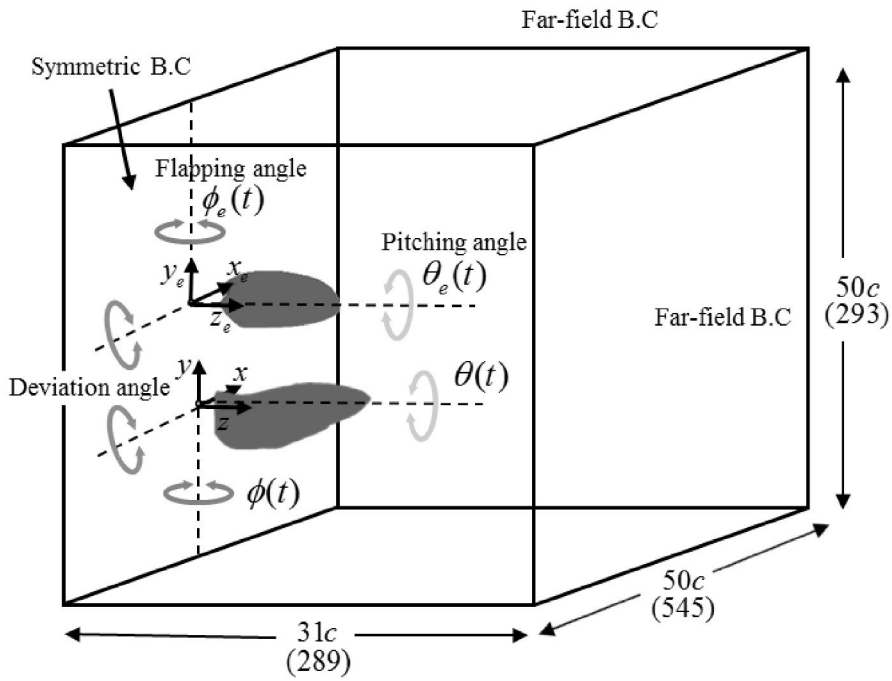


FIGURE 2.2 Computational domain and grid distribution

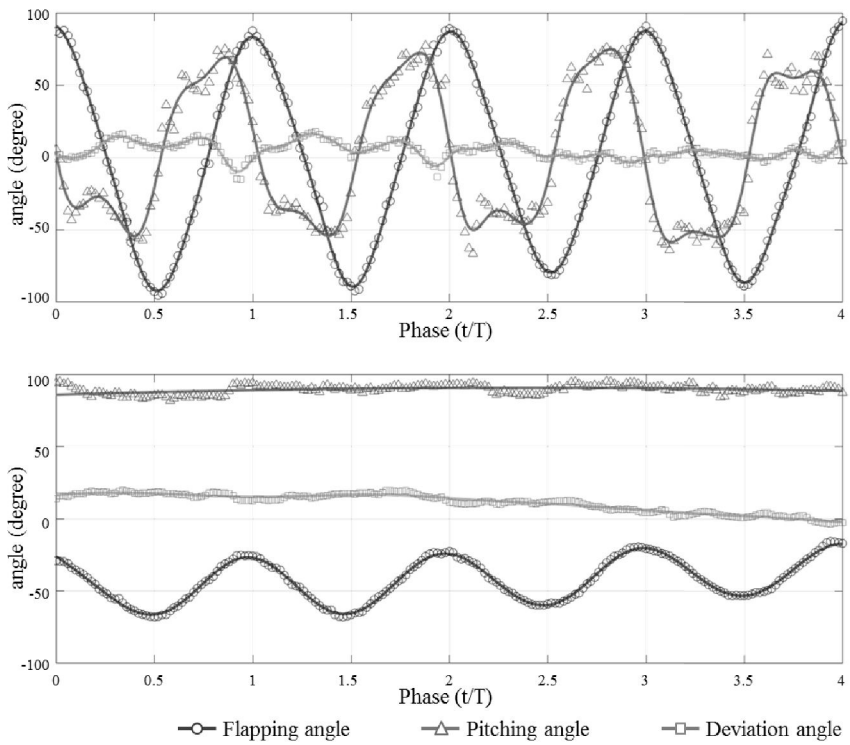


FIGURE 2.3 Measured wing kinematics

Chapter 3

Numerical Results and Discussion

3.1 Vortical structures and force coefficients

Figure 3.1 shows the vortical structures based on λ2 criterion. It shows the leading edge vortex attached on the upper surface of the hind wing and the wing tip vortex generated at the wing tip. Vortical structures are generated around the elytra, however its size and strength is minor compared to the ones generated from the hind wing. Vortical structures generated from the hind wing of the rhinoceros beetle exhibit more turbulent characteristics compared to that of dragonflies (Kweon, 2010).

Figure 3.3 shows the vertical and horizontal force coefficients generated by the hind wing and the elytron. The solid line, dashed line and dotted line represent the force coefficients generated by the hind wing with the presence of elytra, without the presence of elytra and by the elytra themselves respectively. The vertical and horizontal force coefficients are defined as

$$C_V = \frac{F_V}{\frac{1}{2}\rho U^2 S} \tag{3.1}$$

$$C_H = \frac{F_H}{\frac{1}{2}\rho U^2 S} \tag{3.2}$$

where F_V and F_H are vertical and horizontal forces respectively, ρ is the density of air, and S is the wing surface area.

Most of the lift force is generated by the hind wing, while the

elytron is generating negligible lift force. Figure 3.3 shows the phase averaged vertical force coefficients of the hind wing. The average vertical force generated by the hind wing over four periods is the same regardless of the presence of the elytra. For both cases, $\bar{C}_V = 0.148$. The reference velocity is defined as $U = \pi\phi_a f \bar{c} \sim 20.4\text{m/s}$, where ϕ_a is the stroke amplitude, and f is the flapping frequency. The produced vertical force generated by a pair of hind wings can be calculated using the equation (3.1). $\bar{F}_V = \rho U^2 S \bar{C}_V = 61.3\text{mN}$, where S is the wing surface area of a pair of hind wings, which is 16.2 cm^2. The weight of the beetle used for the measurement of the wing kinematics is 57.8mN. Therefore enough lift force is generated to lift up the beetle.

3.2 Iso-pressure surface

In order to study the pressure distributions around the wings of the beetle, iso-pressure surfaces are drawn. Figure 3.2 shows the iso-pressure surface viewed from the upper surface of the hind wing during translational motion. The upper three pictures show the iso-pressure surface with the presence of elytra, and the lower three show the iso-pressure surface without of the elytra. The iso-pressure surface represents the region of $p^*=-1.5$, where p^* is the non-dimensionalised pressure. The results were compared at three different phases; the acceleration phase, mid-stroke phase, and deceleration phase. Regions of iso-pressure surface are comparable for the cases with the elytra and without the elytra. Therefore the formation of low pressure regions on the upper surface of the hind wing is undisturbed by the presence of the elytron.

3.3 Vorticity fields at the cross-sections of the hind wing

We have examined the vorticity fields at the cross-section of the hind wing at various span-wise distances to further analyze the interaction between the elytra and the hind wing. Generation and disappearance of the leading edge vortex can be seen throughout the strokes. The vorticity fields near the hind wing are nearly identical with the elytra present and with the elytra absent. Figure 3.4 shows the contours of the instantaneous span-wise vorticity at a span-wise location of R=0.25r during the pronation. The elytron and the hind wing are in close proximity during the pronation, however the generation of leading edge vortex remains undisturbed. Therefore we may conclude that the disturbance caused by the interaction between the elytra and the hind wing to the generation of the leading edge vortex is negligible.

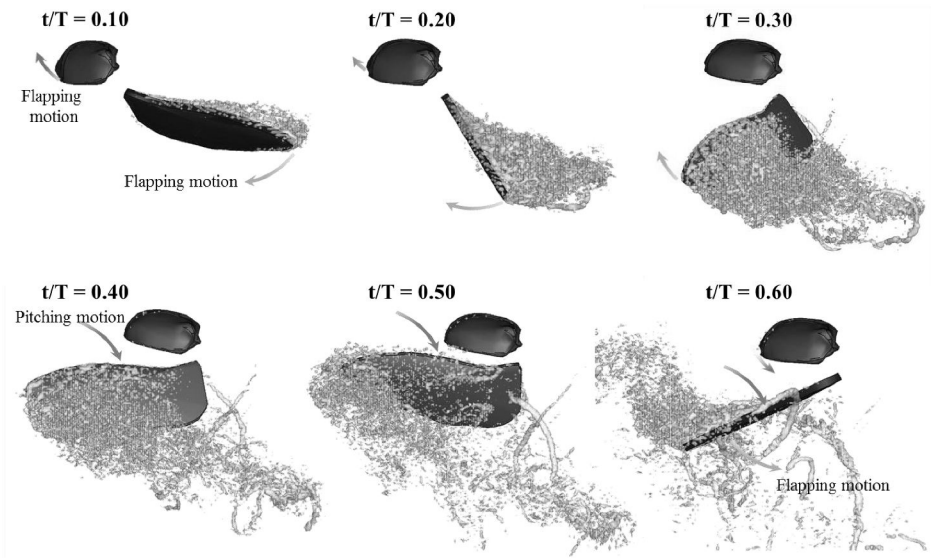


FIGURE 3.1 Instantaneous vortical structures (λ2 vortex definition of Jeong & Hussain) at six different phases

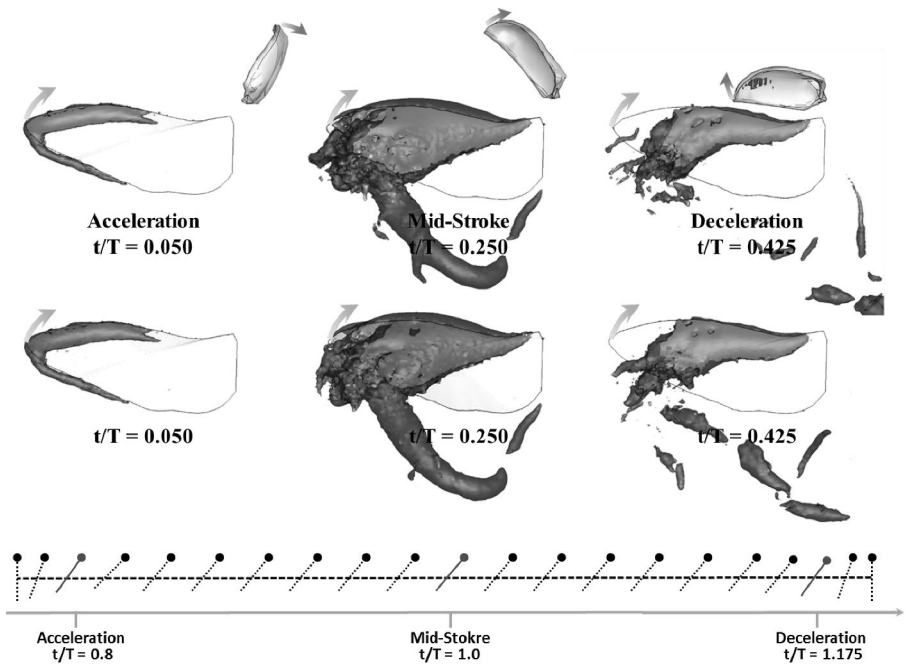


FIGURE 3.2 Iso-pressure surface of $p^*=-1.5$ over the hind wing at three different phases viewed from the upper surface of the hind wing: with the presence of elytra (upper), with the absence of elytra (lower)

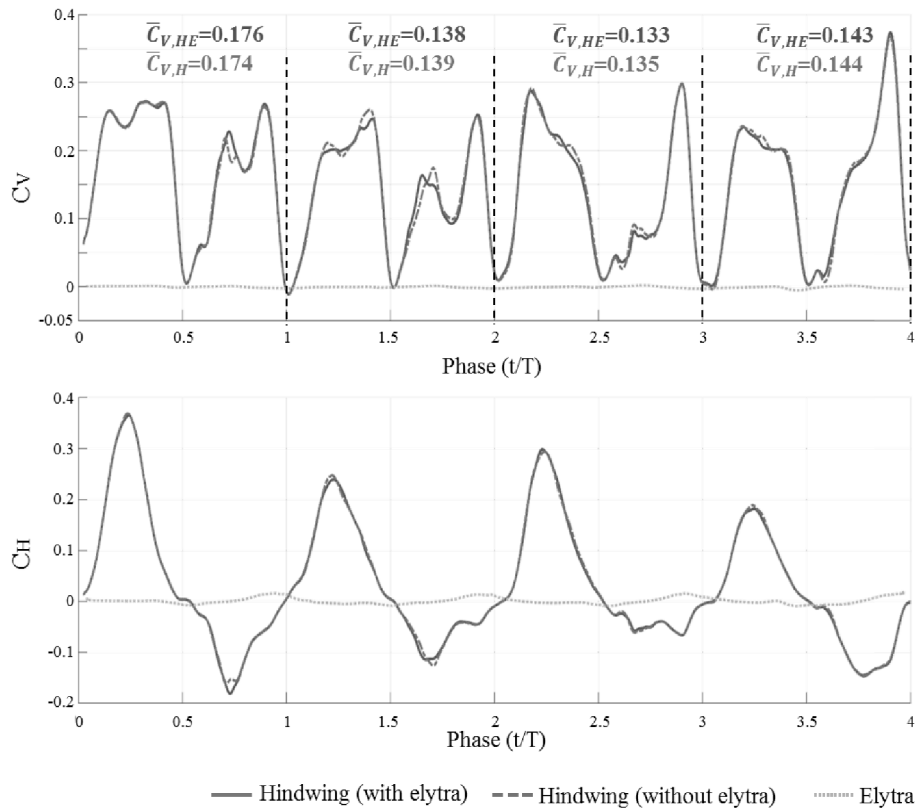


FIGURE 3.3 Time history of vertical force coefficients (upper) and horizontal force coefficients (lower)

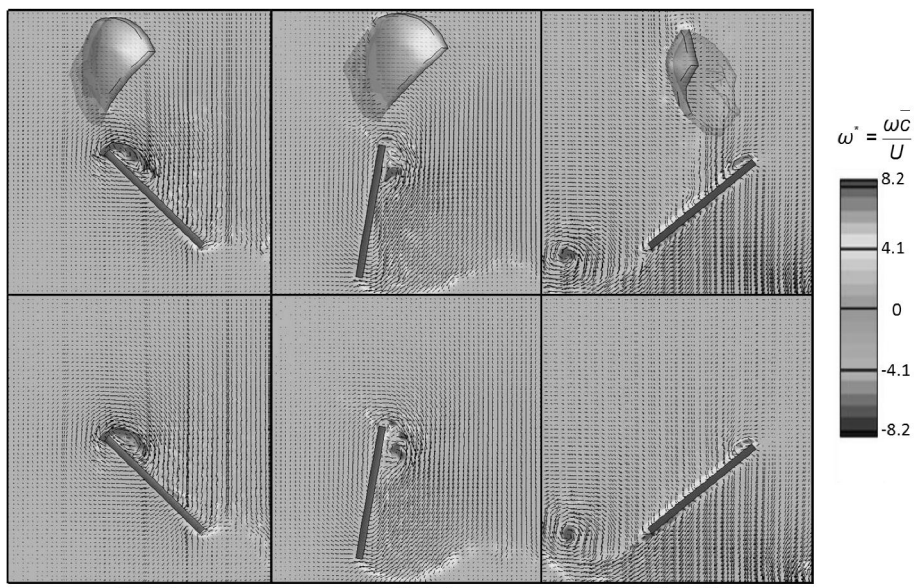


FIGURE 3.4 Contours of the instantaneous span-wise vorticity at a span-wise location of R=0.25r, and their velocity vector during pronation for the case with the elytra (upper), and without the elytra (lower)

Chapter 4

Code Validation

4.1 Experimental setup

In order to validate the numerical simulation results, they were compared with the experimental results. The experiments were performed by Sehyeong Oh (2015). Figure 4.1 shows the computational domain and experimental setup used for validation. In this case, only the hind wing was considered and modeled wing kinematics were used for ease of analysis as shown on figure 4.2. Wing kinematics were modeled using trigonometric functions given as

$$\phi(t) = -\frac{4}{9}\sin\left(2\pi\frac{t}{T}\right) \tag{4.1}$$

$$\theta(t) = \begin{cases} \frac{2}{9}\pi, & 0 < t/T < 0.15 \\ \frac{\pi}{2} + \frac{5}{18}\pi\sin\left(5\pi\left(\frac{t}{T} - 0.25\right)\right), & 0.15 < t/T < 0.35 \\ \frac{7}{9}\pi, & 0.35 < t/T < 0.65 \\ \frac{\pi}{2} - \frac{5}{18}\pi\sin\left(5\pi\left(\frac{t}{T} - 0.75\right)\right), & 0.65 < t/T < 0.85 \\ \frac{2}{9}\pi, & 0.85 < t/T < 1.0 \end{cases} \tag{4.2}$$

where ϕ is the flapping angle and θ is the pitching angle. The deviation angle is assumed to be constant value of 0 ° .

4.2 Validation result

Initially, a grid dependency test was performed to ensure the consistency of simulation results with the variation in grid numbers. Three different numbers of grids were tested, those are 26,899,419 $(N_x, N_y, N_z) = 417 \times 251 \times 257$, 46,148,965 $(N_x, N_y, N_z) = 545 \times 293 \times 289$ and 78,168,431 $(N_x, N_y, N_z) = 737 \times 367 \times 289$ grid points. Figure 4.3 shows the result of the grid dependency test. The resulting vertical and horizontal force coefficient graph exhibits similarity in their trend and an integral error of less than 1% for both vertical force and horizontal force coefficients between each number of grid points used. Therefore it is considered that enough grid points were used.

Secondly, numerical simulation results are validated with the experimental results. The strength of leading edge vortex is compared at a span-wise distance of r=0.5R. At this span-wise distance, it is expected that the strength of leading edge vortex is the maximum. At a further distance along the span-wise direction, the leading edge vortex detaches from the upper surface of the wing during the stroke, therefore comparison becomes more difficult. At a shorter span-wise distance, near the root, the translational velocity is lower; therefore the strength of the leading edge vortex becomes weaker.

The results were compared at three different phases; those are the acceleration phase, mid-stroke phase and deceleration phase. For the comparison, phase averaged data were used. In order to identify the region of leading edge vortex, we have defined the region where $\lambda_2 < 0$ and $\omega_z > 0$. Thus the region of interest shows the vortical structure of positive vorticity and eliminate

vorticity arises from wall shear ($\lambda_2 = 0$) and trailing edge vortex ($\omega_z < 0$). Figure 4.4 shows the leading edge vortex identified from the results from the experiment, and from the numerical simulations at three different phases: the acceleration phase, mid-stroke phase, and deceleration phase.

The graph on figure 4.4 shows the circulation values obtained from the experiment (Γ_{exp}) and from the numerical simulations (Γ_{num}) at three different phases. It shows that the circulation values obtained from the numerical simulations are in good agreement with the values obtained from the experiment. The maximum error is 9%. The maximum error occurs at the acceleration phase. Two hundred eighty instantaneous fields were used for the phase averaging of experimental results, whereas only seven were used for the numerical simulation results. However, figure 4.5 shows the variation of circulation values with the different number of instantaneous fields used is only minor.

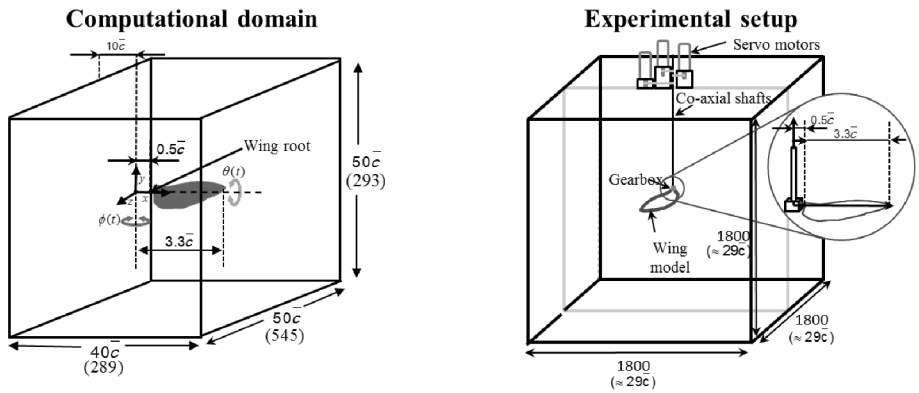


FIGURE 4.1 Computational domain and grid distribution for the code validation and grid dependency test (left) and experimental setup for the code validation (right)

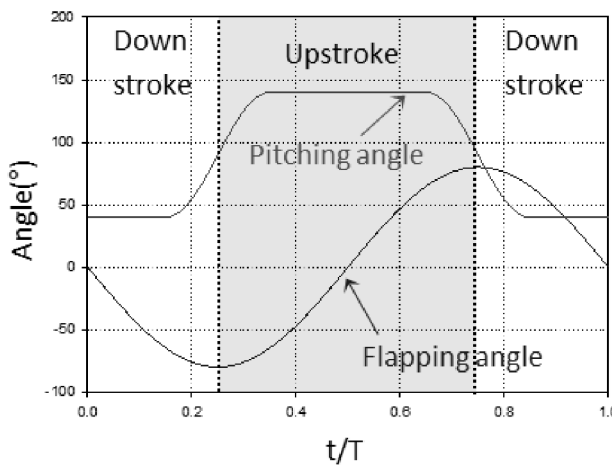


FIGURE 4.2 Modelled wing kinematics implemented for the code validation case and grid dependency test

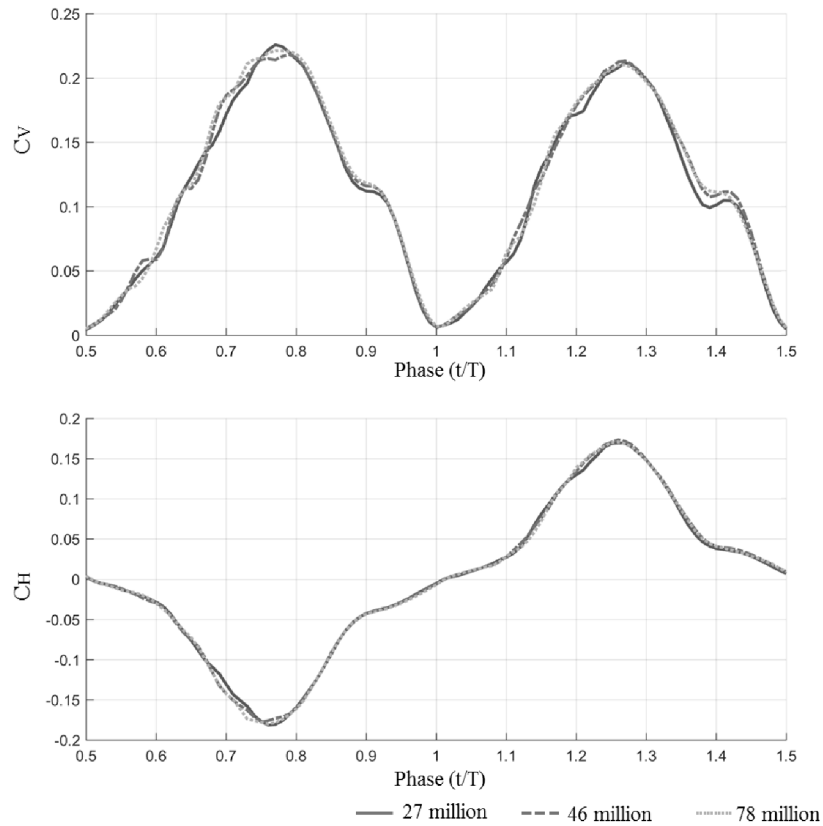


FIGURE 4.3 vertical force coefficient (upper) and horizontal force coefficient obtained for the grid dependency test (lower)

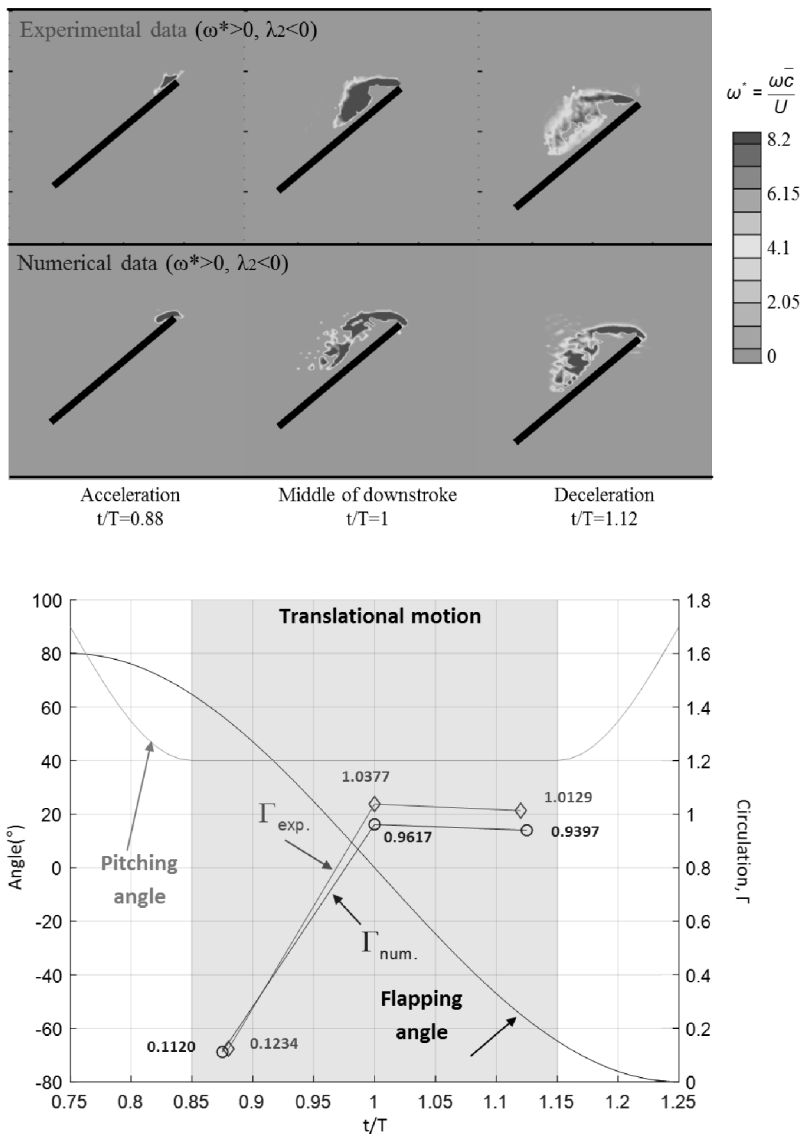


FIGURE 4.4 Leading edge vortex identification at the cross-section of the hind wing (upper), and a graph showing strength of leading edge vortex at three different phases (lower)

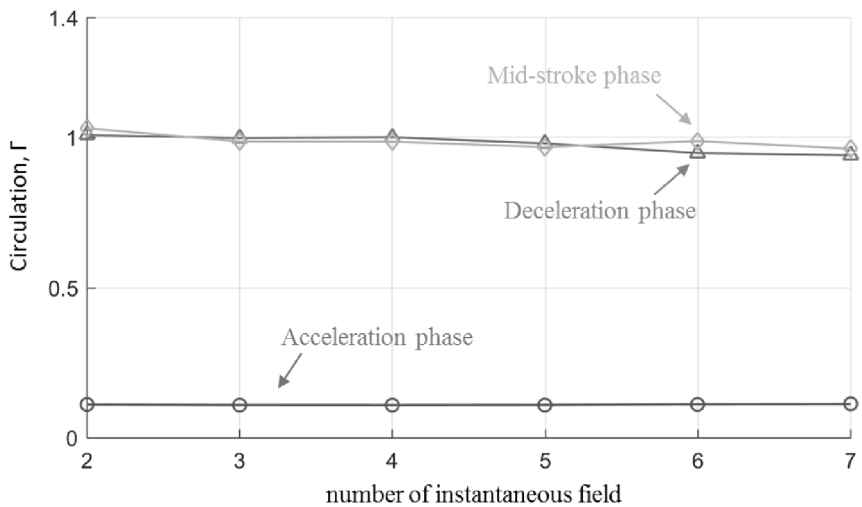


FIGURE 4.5 Variation of circulation values with different number of instantaneous field is used for the phase averaging

Chapter 5

Summary and Conclusion

Numerical simulations were performed to analyze the flow characteristics around the flapping wings of a beetle. With the wing geometries and wing kinematics implemented, it was found that enough lift force was generated to support the weight of the beetle. During take-off, having elytra makes no difference to the generation of vertical and horizontal forces. Therefore the motions of the elytra do not affect the aerodynamic performance of the hind wing during take-off.

The primary function of the elytra is the protection of the hind wing when not flying. Therefore it would be advantageous for a beetle to have elytra as they protect the hind wing when folded, and they do not disturb the lift force generated by the hind wing during the flight.

Bibliography

Ho, S., Nassef, H., Pornsinsirirak, N., Tai, Y. C., & Ho, C. M. (2003). Unsteady aerodynamics and flow control for flapping wing flyers. Progress in Aerospace Sciences, 39(8), 635-681.

Spedding, G. R., & Lissaman, P. B. S. (1998). Technical aspects of microscale flight systems. Journal of Avian Biology, 458-468.

Tennekes, H. (2009). The simple science of flight: from insects to jumbo jets. MIT press.

Lu, Y., & Shen, G. X. (2008). Three-dimensional flow structures and evolution of the leading-edge vortices on a flapping wing. Journal of Experimental Biology, 211(8), 1221-1230.

Ellington, C. P. (1984). The aerodynamics of hovering insect flight. I.-IV. Philosophical Transactions of the Royal Society B: Biological Sciences, 305, 1.

Ellington, C. P., Van Den Berg, C., Willmott, A. P., & Thomas, A. L. (1996). Leading-edge vortices in insect flight.

Sun, M., & Tang, J. (2002). Unsteady aerodynamic force generation by a model fruit fly wing in flapping motion. Journal of Experimental Biology, 205(1), 55-70.

Dickinson, M. H., Lehmann, F. O., & Sane, S. P. (1999). Wing rotation and the aerodynamic basis of insect flight. Science, 284(5422), 1954-1960.

Medina, A., Eldredge, J. D., Kweon, J., & Choi, H. (2015). Illustration of Wing Deformation Effects in Three-Dimensional Flapping Flight. AIAA Journal, 1-14.

Kim, J., Kim, D., & Choi, H. (2001). An immersed-boundary finite-volume method for simulations of flow in complex geometries. Journal of Computational Physics, 171(1), 132-150.

Kweon, J. (2011) Three-dimensional Vortical Structures around the Flapping Insect Wings. Ph.D thesis, Seoul National University

Lee *et al.*, (2015) Aerodynamics of a beetle in take-off flights, Presented at American Physical Society division of Fluid Dynamics, L27.00010

Oh *et al.*, (2015) Interaction of the elytra and hind wing of a rhinoceros beetle (Trypoxylus dichotomus) during a take-off mode. Presented at American Physical Society division of Fluid Dynamics, L27.00011

Jeong, J., & Hussain, F. (1995). On the identification of a vortex. Journal of fluid mechanics, 285, 69-94.

Birch, J. M., & Dickinson, M. H. (2001). Spanwise flow and the attachment of the leading-edge vortex on insect wings. Nature, 412(6848), 729-733.

이륙 비행 하는 장수풍뎅이의 겉날개-속날개 상호작용

서울대학교 대학원
기계항공공학부
오승영

요 약

장수풍뎅이의 날개는 겉날개와 속날개 두쌍으로 이뤄져있다. 딱딱한 겉날개는 비행하지 않을 시에 배를 덮어 장수풍뎅이의 배와 속날개를 보호하는 역할을 한다. 이륙비행을 준비 할 시에 겉날개가 먼저 펼쳐지게 되며, 이후에 속날개와 함께 같은 주기로 퍼덕인다. 본 연구에서는 장수풍뎅이의 이륙비행시 퍼덕이는 겉날개와 속날개의 상호작용에 대해 수치해석적으로 분석하였다. 수치해석은 Re=17,000 (속날개의 평균 날개시위길이와 속날개 끝단 최고속도기준)에서 수행하였으며, 가상경계방법(Immersed boundary method)을 사용하여 실행되었다. 본 연구는 장수풍뎅이의 이륙비행에 한해서 수행되었으며, 실제 장수풍뎅이의 이륙비행시 초고속 카메라를 통해 측정된 날갯짓 궤적을 사용하였다. 수치해석을 통해 퍼덕이는 속날개 주위의 3차원 보티컬 구조와 날개 주위의 낮은 압력구간을 가시화 하여 겉날개가 이에 미치는 영향을 살펴보았다. 겉날개 자체로서 생성되는 양력은 극히 미미하며 속날개의 양력생성에 미치는 영향 역시 없는 것으로 확인 되었다.

주요어: 장수풍뎅이, 곤충 날개, 날개 상호작용, 곤충 비행, 이륙비행, 보티컬 구조, 양력, 서큘레이션

학번: 2014-21568